IOP Publishing J. Phys. D: Appl. Phys. 59 (2026) 095003 https://doi.org/10.1088/1361-6463/ae4995

Journal of Physics D: Applied Physics

PAPER

RECEIVED
22 November 2025

REVISED
11 February 2026

ACCEPTED FOR PUBLICATION
24 February 2026

PUBLISHED
5 March 2026

Theoretical study of the stability and magnetic anisotropy of CrX_3(X = Cl, Br, I) nanotubes

Jing Huang and Yu-Jun Zhao*

Department of Physics, South China University of Technology, Guangzhou 510640, People's Republic of China
* Author to whom any correspondence should be addressed.

E-mail: zhaoyj@scut.edu.cn

Keywords: CrI_3 nanotubes, curvature, magnetic anisotropy

Abstract

Inorganic nanotubes (NTs) derived from two-dimensional materials, especially CrI_3 NTs, exhibit promising application in the fields of spintronics and optical nanodevices due to their unique magnetic and optical properties. Here, the correlation between curvature and formation energy is systematically investigated for CrI_3 NTs with different chiral indices. Further study on the interaction between CrI_3 NTs and the nested carbon NTs (CNTs) reveals that CNT encapsulation can significantly improve the structural stability of CrI_3 NTs. The CrX_3(X = Cl, Br, I) monolayer structure exhibits axial magnetic anisotropy energy (MAE), with its lowest free energy distributed along the *z*-axis. In contrast, CrI_3 NTs with a tube radius ranging from 5 Å to 28 Å show in-plane magnetic anisotropy, where the lowest free energy exists in the *xy*-plane, and the absolute value of the MAE increases as the curvature increases. When the curvature is greater than 0.11, the absolute value of MAE is higher than that of the plane. With further exploration of $CrCl_3$ NTs and $CrBr_3$ NTs, it is found that the MAE of NTs with a tube radius within 28 Å also increases with the increase of compressive strain. Through the analysis of symmetry and orbital contribution of MAE, the physical mechanism behind the differences in magnetic anisotropy is clarified.

1. Introduction

With the rapid global development of informatization and the knowledge economy, the micro–nano electronic device industry has become a key indicator for measuring a country's industrial competitiveness and comprehensive national strength. Next generation micro–nano electronic devices integrating the spin and charge properties of electrons have attracted considerable attention [1, 2]. In recent years, alongside the growing research on micro–nano magnetic systems and two-dimensional (2D) magnetic systems [3, 4], magnetic systems induced by geometric bending have emerged as a new and rapidly developing branch of modern magnetism [5–7]. Magnetic materials with geometrically curved surfaces exhibit magnetic effects regulated by their geometric shapes, thereby giving rise to novel magnetic interactions [8]. Curvature influences the magnetic properties of materials: curved geometries can induce the Dzyaloshinskii–Moriya interaction (DMI) in materials, which is critical for the design of new-type magnetic devices. Studying the magnetism induced by geometric bending and clarifying how shape affects the magnetic behavior of magnetic materials enables better control of magnetic anisotropy. Research on curved magnetic systems holds implications for the development of ultra-fast, energy efficient memories, logic devices, and sensors based on the principles of spin orbit electronics and magnonics. It also opens new avenues for mechanically flexible geometrically curved structures in spintronics, spin orbit electronics of curved magnetic systems, and soft robotics [6, 7].

Progress in the research on curved magnetic systems relies on the development of relevant experimental technologies. Sanchez *et al* [9] reported a novel method combining glancing angle deposition (GLAD) of organic molecules with the vertical growth of inorganic materials. The resulting thin films retain the distinctively clear tilted columnar microstructure characteristic of GLAD, with inorganic materials embedded within the columns. Pacheco *et al* [10] focused on focused electron beam-induced

deposition a direct write nanofabrication technique to pattern three dimensional magnetic nanostructures with a resolution comparable to the characteristic magnetic length scale. Fomin *et al* [11] demonstrated that radially magnetized microhelical coils exhibit two distinct motion modes under parametric magnetic field excitation, driven by the interaction between magnetic torque and damping torque. Wang *et al* [12] grew MoS_2 on the outer surface of carbon nanotubes (CNTs) to prepare high-performance energy materials, yielding stable MoS_2 NTs. Tiwari *et al* [13] also fabricated a molybdenum disulfide (MoS_2) shell on the inner core of molybdenum carbide (Mo_2C) NTs. Caha *et al* [14] successfully prepared CNT encapsulated CrI_3 NTs in experiments. Kaneda *et al* [15] achieved Janus WSSe/WSe_2 heterostructure nanoscrolls with adjustable diameters by controlling the number of layers; notably, nanoscrolls with small-diameters (30 nm) exhibited strong polarization dependence. By investigating CrS_2 NTs and $CrTe_2$ NTs, Li *et al* [16] found that the strain gradient in the NT wall layers can also induce radial polarization, endowing the NTs with both magnetic and polar properties.

The CrX_3 monolayer magnet exhibits a significant magnetothermal effect along with notable strain tunability [17]. Applying compressive strain can substantially boost this magnetothermal response by increasing the overall magnetic moment while simultaneously lowering the Curie temperature. Under tensile strain, the magnetic sequence can transform from antiferromagnetic to ferromagnetic. The ground state of Zr_2N MXene without strain is essentially antiferromagnetic, but when the applied strain is greater than 4%, the magnetization state of Zr_2N MXene tends to be ferromagnetic [18].

The magnetic anisotropy of lanthanide complexes can transition between easy axis and plane configurations [19]. This behavior arises from the remodeling of free energy associated with molecular properties, which is induced by the progressive redistribution of states with varying compositions, thereby endowing the material with directionally switchable characteristics. Some compounds may exhibit various types of magnetic anisotropy, which can be influenced by external stimuli such as temperature, magnetic fields, and pressure [20]. Consequently, the magnetic anisotropy of certain materials should be deliberately tailored to achieve a specific configuration. Recent first-principles calculations have further advanced the study of the curvature strain energy relationship in CrI_3 NTs. Strain induces a direct spin-up and indirect spin-down bandgap in CrI_3 NTs, resulting in anisotropic optical properties and anomalous optical dispersion within the visible spectrum, providing a platform for applications in spintronics and optical nanodevices [21]. Non-collinear spin polarized density functional theory (DFT) has been employed to determine the flexible magnetic coupling coefficients in magnetic CrI_3 NTs, revealing a significant influence of spin orbit interaction on curvature induced anisotropy [22]. Safi *et al* [23] calculated the magnetic anisotropy energy (MAE) of CrI_3 bilayers, showing that CrI_3 BL has an out-of-plane easy axis which remains unchanged over the entire applied strain range, with most of the contribution to the perpendicular magnetic anisotropy coming from iodine atoms.

Despite significant progress in experiments and theories, research on magnetism in geometrically curved structures still faces challenges. Within the framework of DFT, curvature disrupts translational symmetry. The study of NTs often requires large periodic supercells containing hundreds of atoms; moreover, calculating DMI involves spin orbit coupling (SOC) and non-collinear magnetism, making this a complex task. Additionally, to enhance the feasibility of experimentally preparing curved magnetic systems, theoretical calculations can screen suitable candidate materials by evaluating thermodynamic and kinetic stability. However, in this study, due to the large number of atoms in the NTs, calculations of kinetic stability was not conducted. In terms of theoretical calculations, computational simulations of magnetic NTs are still mostly limited to the CrI_3 system. Further research on more systems is needed to deepen understanding of the interactions induced by curved geometries, thereby facilitating the construction of stable, high-performance magnetic NTs with strong anisotropy.

Studying the stability and MAE of ferromagnetic CrX_3 NTs with different curvatures is conducive to the design and fabrication of next generation high-performance micro–nano spintronic devices. The study of 2D magnetic material NT stability is a complex and challenging field. For single-walled CrI_3 NTs, theoretical calculations show that when the NT diameter exceeds 45 Å, the average strain energy per molecular formula can be reduced to below 50 meV which is a key condition for forming a stable curved magnetic system [24]. Currently, experiments have successfully prepared CNT encapsulated CrI_3 NTs, indicating that CNT encapsulation can enhance the stability of CrI_3 NTs. MAE refers to the difference in a material's ability to be magnetized along different directions, which is crucial for magnetic storage devices and spintronic applications. Chirality affects the physical properties of magnetic NTs and is also closely associated with MAE. Gaining in-depth insight into the relationship between chirality, curvature, and MAE not only enhances understanding of magnetic interaction models but also guides the design of magnetic systems with specific magnetic properties. For instance, optimizing the MAE of NTs by adjusting their curvature enables precise control of the magnetic state.

Table 1. $CrBr_3$ NTs structural parameters (armchair type (n,n)).

System	Radius (Å)	Lattice $a=b$ (Å)	Average bond length (Å)	Average bond angle (°)
$CrBr_3$ (6,6)	10.66	32.328	2.493	99.6
$CrBr_3$ (8,8)	14.21	40.923	2.498	98.0

Table 2. $CrCl_3$ NTs structural parameters (armchair type (n,n)).

System	Radius (Å)	Lattice $a=b$ (Å)	Average bond length (Å)	Average bond angle (°)
$CrCl_3$ (6,6)	10.03	31.029	2.334	99.7
$CrCl_3$ (8,8)	13.37	40.853	2.337	98.4

This study addresses the lack of a stability theory for CrI_3 NTs by using first-principles calculations to evaluate how encapsulation within CNT affects their structural and magnetic stability. Encapsulation significantly lowers the adsorption energy of CrI_3 NTs, enhancing their stability through favorable interactions with the CNT. The research systematically explores how tube diameter, chirality, and carbon coatings influence both stability and MAE. The findings show that MAE increases with curvature, surpassing that of planar CrI_3 when curvature exceeds 0.11. Similar trends are observed in $CrCl_3$ and $CrBr_3$ NTs under compressive strain. The study attributes these effects to symmetry changes and orbital contributions, offering insight into how geometric bending enhances magnetic anisotropy. These results provide a theoretical foundation for designing stable, high-anisotropy magnetic NTs and extend the approach to other 2D magnetic materials. The work supports future applications in energy storage, conversion, and magnetic nanotechnology.

2. Computational methods and models

2.1. NT construction model

The layered structure of the bulk CrX_3 unit cell was optimized using the Perdew Burke Ernzerhof (PBE) functional. As shown in figure 1(a) the equilibrium geometry of CrI_3 yields cell vectors ($a=6.938$ Å, $b=6.941$ Å) in good agreement with experimental values ($a=6.867$ Å, $b=6.867$ Å) [25]. The angles are $\alpha=90°$, $\beta=90°$, $\gamma=120°$. The NT radius is defined as:

$$R=\frac{a}{2\pi}\sqrt{n^2+nm+m^2}. \tag{1}$$

As shown in figures 1(d) and (c), CrI_3 NTs with different chiral indices, where n and m are the chiral indices, $(n,0)$ zigzag and (n,n) armchair types. The resulting NTs are shown in the figure below, with $\alpha=90°$, $\beta=90°$, $\gamma=90°$. One stable configuration for the planar heterostructure is achieved by matching a 1×1 CrI_3 monolayer with a $\sqrt{7}\times\sqrt{7}$ graphene supercell; the other is achieved by matching a $\sqrt{3}\times\sqrt{3}CrI_3$ monolayer with a 5×5 graphene supercell [26, 27]. Based on this matching, NTs were constructed. Heterostructures with smaller tube diameters were selected for the first-principles calculation of adsorption energy. The MAE of CrI_3 NTs with different diameters was calculated and compared with that of the planar structure.

As shown in figure 1(b) the lattice parameters ($a=6.440$ Å, $b=6.440$ Å) are in good agreement with the published theoretical result of $CrBr_3$ monolayers ($a=6.306$ Å, $b=6.306$ Å) [28]. The angles are $\alpha=90°$, $\beta=90°$, $\gamma=120°$. As shown in figure 1(g), $CrBr_3$ NTs are armchair types. The structural parameters of $CrBr_3$ NTs (armchair type) is listed in table 1. The angles are $\alpha=90°$, $\beta=90°$, $\gamma=90°$. The Cr–Br bond length (2.520 Å) matches the theoretical value of $CrBr_3$ monolayers (2.52 Å) [29] and is close to the experimental bulk value (2.52 Å) [30]. The Cr–Br–Cr angle is calculated to be 95.1°, which is consistent with other literature data [31].

As shown in figure 1(c) the lattice parameters ($a=6.053$ Å, $b=6.053$ Å)) are slightly larger than the experimental bulk value ($a=5.959$ Å, $b=6.114$ Å) [32]. The angles are $\alpha=90°$, $\beta=90°$, $\gamma=120°$. As shown in figure 1(h), $CrCl_3$ NTs are armchair types. The structural parameters of $CrCl_3$ NTs (armchair type) is listed in table 2. The angles are $\alpha=90°$, $\beta=90°$, $\gamma=90°$. The Cr–Cl bond length (2.357 Å) is consistent with the value of bulk $CrCl_3$ (2.36 Å) [33]. The Cr–Cl–Cr angle is calculated to be 95.7°, which is consistent with other literature data [34].

2.2. Computational details

We performed the *ab initio* simulations within the DFT [35, 36] framework using the Vienna *ab initio* simulation package [37–40]. Exchange correlation interactions were treated with the generalized

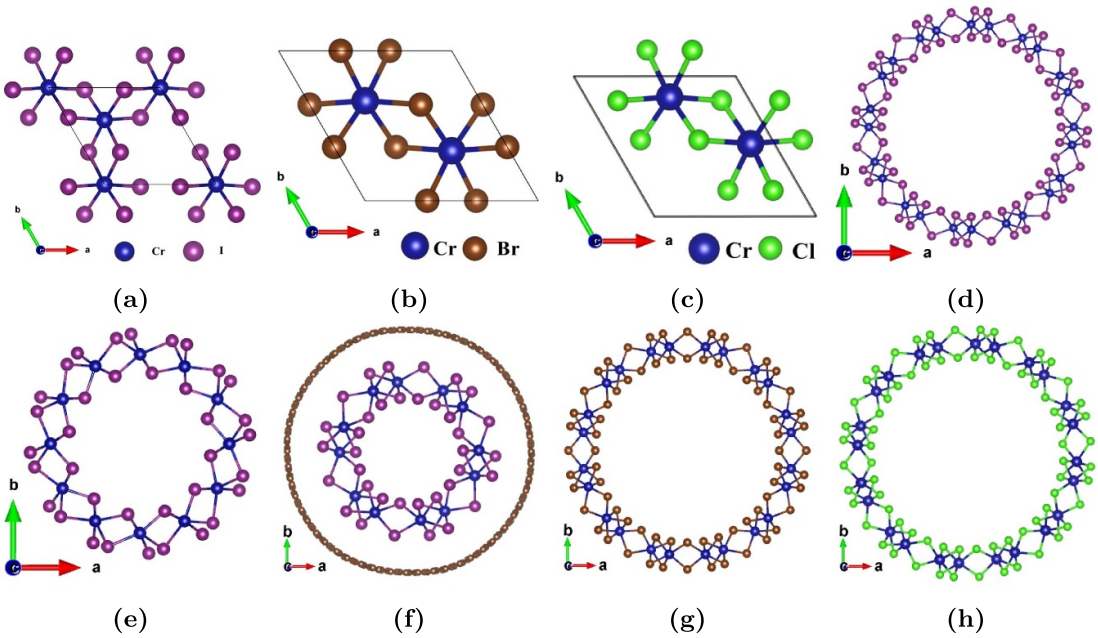

Figure 1. Structural construction of CrX_3. (a), (b) and (c) correspond to planar structure of CrI_3, $CrBr_3$ and $CrCl_3$. (d), (g), and (h) correspond to CrI_3 NTs, $CrBr_3$ NTs, and $CrCl_3$ NTs with a chiral index of $(6,6)$, respectively. (e) The CrI_3 NTs with a chiral index of $(6,0)$. (f) Heterostructure of $(3,3)CrI_3NT@(24,6)CNT$.

gradient approximation within the PBE formulation [41, 42]. The full potential projected plane wave framework [43, 44] was used with an energy cut-off of 600 eV for the plane wave basis set. We optimized the structure until the force on each atom was smaller than 1.5×10^{-2} eV Å^{-1} and the energy convergence reached up to 10^{-6} eV/atom, using the conjugate gradient method. The Brillouin zone was sampled using the Monkhorst–Pack scheme using a $1 \times 1 \times 4$ k-point mesh for atomic and electronic relaxations. A comparison of strain energy in CrI_3 NT structural optimizations with and without the Hubbard U parameter revealed that the U value does not significantly affect the strain energy [24]. In the DFT + U formalism, the Coulomb repulsion has minimal impact on the fundamental band gap value and edge composition. Therefore, U was not included in the structural optimizations performed in this study. Structural optimization was performed using DFT-D3 van der Waals correction. Compared with antiferromagnetic NTs, ferromagnetic NTs have lower energy [14], so all NTs studied in this paper are set to the ferromagnetic state.

2.3. Stability criterion

The formation energy of the CrI_3 NTs is calculated as:

$$E(\mathrm{CrI_3NT}) = E_{\mathrm{total}} - n_{\mathrm{Cr}}E_{\mathrm{Cr}} - m_{\mathrm{I}}E_{\mathrm{I}}. \tag{2}$$

The strain energy refers to the energy difference between the CrI_3 NTs and its planar counterpart, where CrI_3 is the formation energy of CrI_3 monolayer.

$$E(\mathrm{strain}) = E_{\mathrm{CrI_3}NT} - E_{\mathrm{CrI_3plane}}. \tag{3}$$

The adsorption energy is calculated as:

$$E_{\mathrm{ads}} = E_{\mathrm{substrate+adsorbate}} - E_{\mathrm{substrate}} - E_{\mathrm{adsorbate}} \tag{4}$$

where E_{total} is the total energy of the NT, n_{Cr} is the number of Cr atoms, m_{I} is the number of I atoms, E_{ads} is the adsorption energy of the CNT, $E_{\mathrm{substrate+adsorbate}}$ is the total energy of the heterostructure, and $E_{\mathrm{substrate}}$ and $E_{\mathrm{adsorbate}}$ are the total energies of the individual isolated structures. Effective formation energy of interaction for a CNT encapsulated CrI_3 NTs is defined as:

$$E(\mathrm{CrI_3NT@CNT}) = E(\mathrm{CrI_3NT}) + E_{\mathrm{ads}} \tag{5}$$

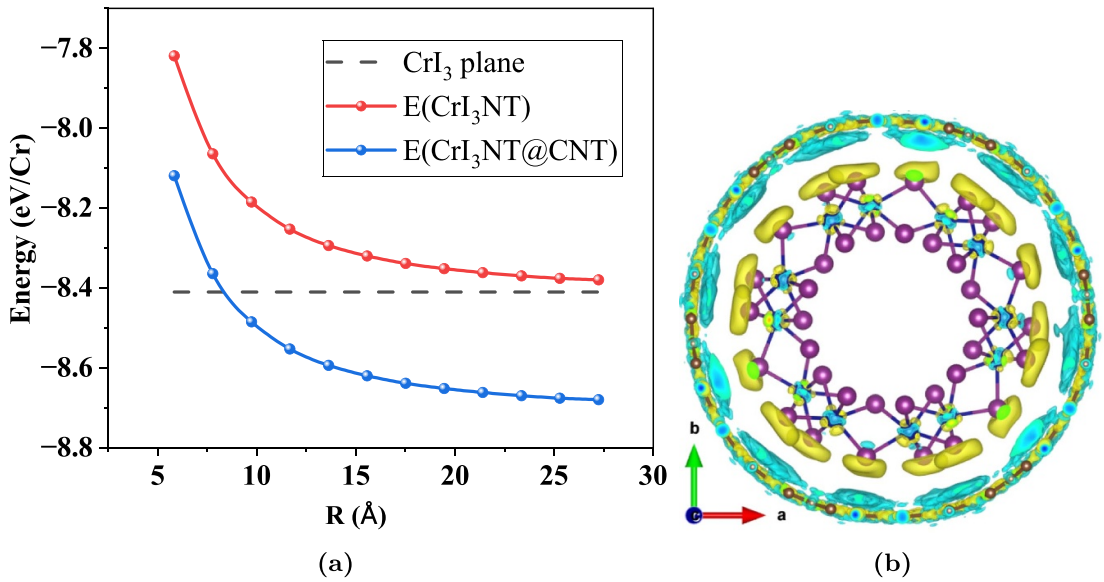

Figure 2. (a) Formation energy of CrI_3 NTs with a chiral index of (n, n). (b) The differential charge density map of $(3,3)CrI_3NT@(24,6)CNT$. Yellow represents the electron accumulation regions, and cyan/green represents the electron depletion regions.

where $E(CrI_3NT)$ is the formation energy of the CrI_3 NTs. The magnetic anisotropic energy was calculated using first-principles methods with SOC by comparing the total energies for different magnetization directions. The MAE is defined as the energy difference between the magnetization aligned along the xy-axis and the z-axis,

$$\mathrm{MAE} = E_{xy} - E_z \tag{6}$$

where E_{xy} is the total energy when magnetic moments are aligned in the xy-plane, and E_z is the energy along the z-axis. A negative MAE indicates in-plane easy axis (xy-plane), consistent with the table, while a positive value of MAE indicates that the z-axis is the easy axis of magnetization

The relationship between curvature and radius is as follows,

$$\kappa = \frac{1}{R}. \tag{7}$$

3. Results and discussion

3.1. CNT encapsulation enhancement

We calculated the formation energies of CrI_3 NTs with chiral indices ranging from $(3,3)$ to $(14,14)$, corresponding to tube radii of 5–28 Å. When we use a 1×1 supercell of the monolayer CrI_3 on a $\sqrt{7} \times \sqrt{7}$ supercell of graphene system, the planar adsorption energy is -11.5 meV per Cr atom. We roll it into $(3,3)CrI_3NT@(24,6)CNT$ using the method, the adsorption energy is -52 meV per Cr atom. Similarly, we roll it into $(5,0)CrI_3NT@(22,11)CNT$ NTs using the method, the adsorption energy is -56 meV per Cr atom. These results indicate that the $(5,0)CrI_3NT@(22,11)CNT$ configuration is more favorable for stabilizing CrI_3 NTs than $(3,3)CrI_3NT@(24,6)CNT$ configuration. Notably, the adsorption energy between NTs is nearly five times that of planar structures, confirming a stronger adsorption effect in the NT system. Thus, the effective formation energy of CNT wrapped CrI_3 NTs is lower than that of planar CrI_3. The formation energy of single-wall CrI_3 NTs is higher than that of the planar CrI_3 structure in figure 2(a). When the tube diameter is less than 10 Å, even though carbon tube coating can reduce the formation energy of CrI_3 NTs, the formation energy of CNT coated CrI_3 NTs is still higher than that of their planar structure. Therefore, under this condition, compared with the planar structure, CrI_3 NTs cannot exist stably. When the tube diameter exceeds 10 Å, the formation energy of CrI_3 NTs encapsulated by CNT becomes lower than that of their planar structure. Under this condition, we consider that CrI_3 NTs can exist stably.

Beyond stability analysis based on formation energy, differential charge density maps of CNT coated CrI_3 NTs reveal interfacial charge transfer with its intensity directly correlated to both adsorption energy magnitude and structural stability. Figure 2(b) illustrates the in-plane charge distribution and structural

Table 3. The tube diameter of CrX_3 (X = Cl, Br, I), MAE, formation energy of single wall CrX_3, and easy-axis direction of CrX_3. A positive MAE value indicates that the energy of the *x*-axis is higher than that of the *z*-axis, while a negative MAE value means the energy of the *x*-axis is lower than that of the *z*-axis. '*z*' denotes that the easy-axis direction is the *z*-axis, and '*xy*-plane' represents that the easy-axis direction lies in the *xy*-plane.

System	Radius (Å)	MAE (meV/Cr)	Formation energy (eV/Cr)	Easy axis
$CrCl_3$-plane	/	0.035	−11.215	*z*-axis
$CrCl_3(6,6)$	10.03	−0.020	−11.131	*xy*-plane
$CrCl_3(8,8)$	13.37	−0.018	−11.204	*xy*-plane
$CrBr_3$-plane	/	0.219	−9.870	*z*-axis
$CrBr_3(6,6)$	10.66	−0.135	−9.777	*xy*-plane
$CrBr_3(8,8)$	14.21	−0.119	−9.849	*xy*-plane
CrI_3-plane	/	0.860	−8.400	*z*-axis
$CrI_3(3,3)$	5.84	−0.950	−7.819	*xy*-plane
$CrI_3(4,4)$	7.78	−0.959	−8.064	*xy*-plane
$CrI_3(5,5)$	9.73	−0.831	−8.185	*xy*-plane
$CrI_3(6,0)$	6.74	−0.574	−8.012	*xy*-plane
$CrI_3(6,6)$	11.68	−0.751	−8.253	*xy*-plane
$CrI_3(7,7)$	13.62	−0.674	−8.294	*xy*-plane
$CrI_3(8,0)$	8.99	−0.536	−8.158	*xy*-plane
$CrI_3(8,8)$	15.57	−0.665	−8.320	*xy*-plane
$CrI_3(9,9)$	17.51	−0.596	−8.339	*xy*-plane
$CrI_3(10,10)$	19.46	−0.554	−8.352	*xy*-plane
$CrI_3(11,11)$	21.40	−0.525	−8.362	*xy*-plane
$CrI_3(12,12)$	23.35	−0.500	−8.370	*xy*-plane
$CrI_3(13,13)$	25.29	−0.491	−8.376	*xy*-plane
$CrI_3(14,14)$	27.24	−0.482	−8.380	*xy*-plane

matching between CNT and CrI_3 NTs. Obvious charge redistribution occurs at their interface, electron density increases on the CrI_3 NTs surface while decreasing on the CNT surface, indicating electron transfer from CNT to CrI_3. The electronegativity of I atoms is 2.66, which corresponds to the main distribution of the yellow region in the figure 2(b), indicating a significant tendency to gain electrons. The electronegativity of carbon atoms in CNT is 2.55, slightly lower than that of I atoms. Therefore, the C atoms exhibit electron-loss characteristics in the interface region. The electronegativity of Cr atoms is 1.66, which is significantly lower than that of I and C atoms. However, since Cr exists in the +3 oxidation state in CrI_3, the ionic bond characteristics of Cr result in a weak degree of electron transfer, leading to no obvious electron-gain or electron-loss behavior. More significant charge transfer leads to stronger interfacial interaction and a larger absolute value of adsorption energy. From the spatial distribution range and intensity of charge density, distinct electron rearrangement at the interface confirms strong adsorption capacity and tight structural bonding. This charge transfer reduces the total system energy and enhances the interfacial pinning effect, thereby endowing CNT coated CrI_3 NTs with high stability.

We extended this model to Cr trihalides (CrX_3(X = Cl, Br, I)). Calculations show that in table 3: for planar CrX_3, formation energy increases with the atomic number of the halide; for CrX_3 NTs, formation energy decreases with increasing tube diameter, approaching that of planar CrX_3 as the diameter tends to infinity. Given that relatively unstable CrI_3 NTs can be stabilized by CNT wrapping, we infer that $CrBr_3$ and $CrCl_3$ NTs can also achieve stable structures via CNT wrapping. While molecular dynamics simulations and phonon spectroscopy are standard techniques for stability evaluation, we did not apply them to CrI_3 NTs. This is because larger CrI_3 NTs diameters though improving stability toward that of planar structures require more atoms in the simulation system, leading to excessive computational resource consumption. Overall, this study demonstrates that reducing formation energy via CNT wrapping is a theoretically viable strategy for enhancing the stability of CrI_3 NTs.

3.2. Correlation between curvature and MAE

MAE is a pivotal parameter governing the magnetic ground state stability and spin manipulation performance of low dimensional magnetic materials. Its magnitude and anisotropy mode directly dictate the storage density and operational efficiency of nanospintronic devices. As shown in table 4, the calculated values of the magnetic anisotropy of CrI_3, $CrBr_3$, and $CrCl_3$ are compared with the published values. For monolayer systems, theoretical results are consistent with experiments within error bars, verifying the reliability of our computational method. For NTs, no direct experimental MAE data exists, but our curvature-dependent MAE trend aligns with the experimental finding that CNT encapsulation enhances magnetic stability of CrI_3 NTs [14]. The negative MAE values (in-plane anisotropy) for NTs

Table 4. MAE comparison.

System	This work (meV/Cr)	Published MAE (meV/Cr)
$CrCl_3$ monolayer	0.035	0.025 [17]
$CrBr_3$ monolayer	0.219	0.160 [17]
CrI_3 monolayer	0.860	0.804 [17]
CrI_3 (6, 6) NTs	−0.751	−0.740 [19]

differ from positive MAE (axial anisotropy) of monolayers, which is attributed to curvature-induced orbital hybridization rearrangement. CrX_3 NTs exhibit pronounced size dependence, chirality dependence, and curvature sensitivity in their MAE in table 3.

As shown in figure 3(d) the absolute value of MAE for CrI_3 (n, n) NTs as a function of curvature κ. When $\kappa > 0.11$ (radius < 9.09 Å), the absolute MAE of NTs exceeds that of the planar CrI_3 (0.860 meV/Cr), indicating shape-induced magnetic anisotropy enhancement. This trend is attributed to curvature-driven orbital hybridization and SOC strengthening. This unique magnetic response arises from the synergistic interplay between structural stability and curvature effects. In-depth elucidation of its intrinsic mechanism holds significant implications for advancing low-dimensional magnetism research and guiding nanospintronic device design.

3.2.1. Curvature effect: the core driver of MAE variation and anisotropy transition

The Cr sublattice separates into two groups of Cr atoms strictly located on the C atoms or C hexagons of the encapsulating CNT. This arrangement between CrI_3 and graphene suppresses the degeneracy of Cr^{3+} ions in the AB alternation. Upon rolling into a NT, CrX_3 retains its core symmetry, the highest symmetry direction is along the NT axis. The *xy*-plane, perpendicular to the *z*-axis, possesses in-plane rotational symmetry, making all in-plane directions symmetry equivalent. When the magnetic moment is aligned along the *z*-axis, the crystal field, orbital hybridization, and local environment differ from those within the plane. Due to the equivalence of all directions within the *xy*-plane, the energy change upon rotating the magnetic moment within the plane is minimal, resulting in an MAE close to zero within the plane.

The crystal field of planar CrI_3 causes the splitting of the d_{xy}, d_{xz}, and d_{yz} orbitals as shown in figure 3(a), and the SOC further enhances the dominant role of these orbitals in the MAE. The curved surface structure of CrI_3 NTs with large curvature as shown in figure 3(b) introduces strong structural distortion, which changes the crystal field environment of Cr atoms. The SOC effect of the d_{xy} orbital is greatly enhanced, and it shifts from a positive contribution in the planar structure to a strong negative contribution in the NT structure, thereby dominating the magnetic anisotropy of the system. The structure of NTs with small curvature as shown in figure 3(c) is closer to that of the planar structure. Thus, the orbital contributions are more dispersed. The dominant role of d_{xy} is weakened, while the contributions of d_{yz}, d_{z^2}, and $d_{x^2-y^2}$ begin to emerge, and the overall strength of the MAE is also significantly reduced.

As an intrinsic structural parameter of NTs, curvature directly governs the numerical evolution and mode transition of MAE by reconstructing electronic orbital hybridization, modulating SOC strength, and altering magnetic moment alignment patterns. When the tube diameter falls within 5–28 Å, high curvature drastically disrupts the hexagonal symmetry of planar CrX_3, inducing two distinct magnetic effects. On one hand, curvature drives directional hybridization of Cr*d*-orbitals and X*p*-orbitals along the *z*-axis, leading to a far higher degree of electron cloud localization along the NT axis than in the radial direction. According to the minimum energy principle, magnetic moments tend to align along the *z*-axis where electron localization is strongest, yielding the easy axis magnetic anisotropy defined along the *z*-axis in figure 4(a) and the *xy*-plane, which is fundamentally distinct from the easy planar behavior of planar CrX_3 in figure 4(b). On the other hand, high curvature causes Cr–X bond angles to deviate from the equilibrium values of planar structures, enhancing the SOC effect of Cr atoms. Notably, for the heavy halogen I, its robust SOC property further amplifies this curvature induced MAE enhancement, resulting in a monotonic increase in the absolute MAE as curvature rises. This trend holds across $CrCl_3$, $CrBr_3$, and CrI_3 systems, confirming the universal regulatory role of curvature in MAE.

When the diameter of CrI_3 NTs exceeds 28 Å, their curvature decreases significantly, the axial directionality of orbital hybridization weakens, and the directional preference of electron localization disappears accordingly.

Simultaneously, the magnetic moment alignment mode transitions from axial easy axis orientation to radial inward distribution, forming a vortex like closed magnetic structure. This reduces the total energy

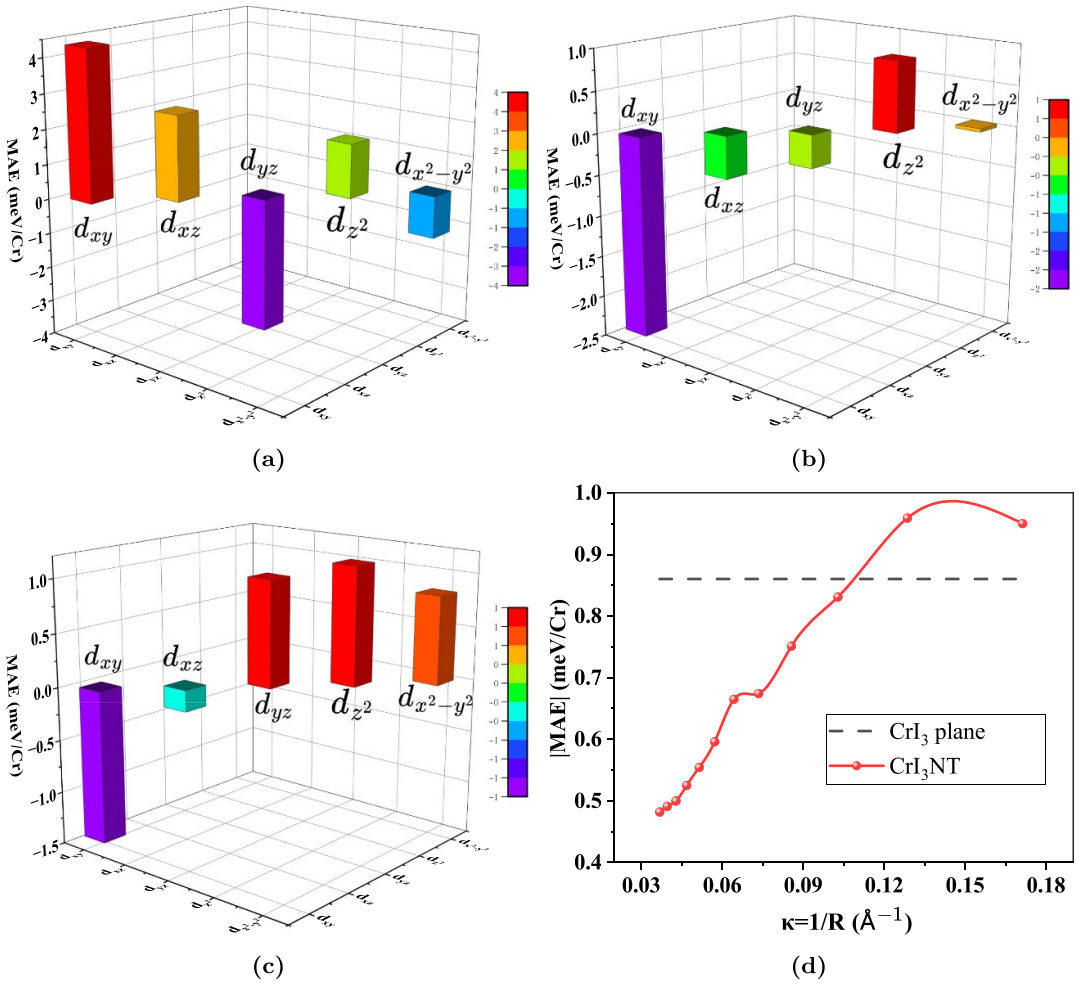

Figure 3. The orbital contribution of MAE of Cr atoms in the CrI_3 plane (a), the $CrI_3(3,3)$ NTs (b), and $CrI_3(6,6)$ NTs (c), respectively. MAE of CrI_3 (n,n) NTs and the MAE of the CrI_3 plane is shown in plot (d).

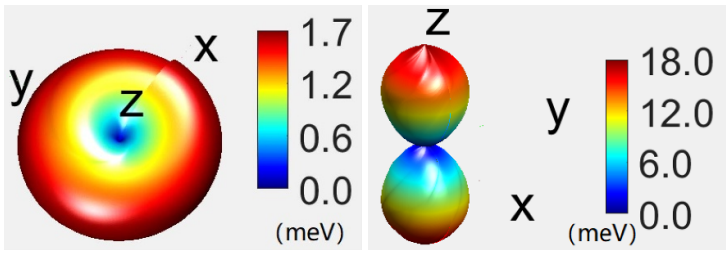

Figure 4. The magnetic anisotropy shape of the planar CrI_3 (a), and $CrI_3(6,6)$ NTs (b), respectively.

and drives the net magnetic moment toward zero. During this transition, the absolute MAE undergoes a change at the critical tube diameter corresponding to the magnetic ground state. When the diameter is smaller than the critical value, the magnetic moment remains oriented along the z-axis, and the absolute value of the MAE increases as the curvature increases. For diameters larger than the critical value, magnetic moments adopt radial inward distribution, and the absolute MAE increases as curvature decreases. Eventually, as the tube diameter approaches infinity, the MAE rises to match that of planar CrI_3, with the magnetocrystalline anisotropic shape transitioning from easy axis to easy plane. The result indicates that the curvature can regulate the MAE of CrI_3 NTs.

3.2.2. Chirality effect: dominated by curvature uniformity

With the same number of constituent atoms, the MAE discrepancy between $(n,0)$ and $(n,n)CrX_3$ NTs stems from chirality induced non-uniform curvature distribution and varying degrees of lattice distortion. For (n,n)-type NTs, atoms are uniformly packed on the tube wall, and curvature maintains a uniform distribution along the circumferential direction. This induces consistent and substantial distortion of Cr–X bonds, fully enhancing z-axis directional hybridization and the SOC effect. For $(n,0)$-type NTs, atoms adopt a periodic zigzag packing, and curvature alternates along the circumferential direction. Local lattice distortions offset one another, weakening the directionality of orbital hybridization and the SOC strength. This chirality induced structural difference directly results in the absolute MAE of $(n,0)$-type NTs consistently being lower than that of (n,n)-type NTs. This rule is independent of halogen type, further confirming the fine-tuning role of curvature uniformity in MAE.

4. Conclusion

In summary, this study demonstrates that CNT encapsulation significantly enhances the stability of CrI_3 NTs by reducing their effective formation energy. Furthermore, a distinct correlation is observed between curvature and MAE in ferromagnetic CrX_3 $(X = Cl, Br, I)$ NTs. The variation in the MAE of CrX_3 NTs stems from the synergistic effect of NT structural stability and curvature. CrX_3 monolayers exhibit axial magnetic anisotropy. The absolute value of MAE of CrX_3 NTs increases as the curvature increases. When the curvature is greater than 0.11, the absolute value of MAE is higher than that of the plane, accompanied by shape induced magnetic anisotropy. As the tube radius approaches the planar limit, the MAE gradually converges toward the value of the corresponding planar structure. This reduction in MAE is attributed to curvature induced strain, symmetry lowering, and orbital hybridization arising from changes in electronic structure. These findings offer valuable insights into the structural stability and magnetic behavior of 2D material-derived NTs, thereby advancing their potential for applications in nanoscale spintronics and energy conversion technologies.

Acknowledgments

This work is financially supported by the National Natural Science Foundation of China (Grant No. 12474229). This work is partially supported by High Performance Computing Platform of South China University of Technology.

Data availability statement

All data that support the findings of this study are included within the article (and any supplementary files).

ORCID iDs

Jing Huang 0009-0001-3036-0782
Yu-Jun Zhao 0000-0002-6923-1099

References

[1] Dieny B *et al* 2020 Opportunities and challenges for spintronics in the microelectronics industry *Nat. Electron.* **3** 446–59
[2] Barla P, Joshi V K and Bhat S 2021 Spintronic devices: a promising alternative to CMOS devices *J. Comput. Electron.* **20** 805–37
[3] Hu G and Xiang B 2020 Recent advances in two-dimensional spintronics *Nanoscale Res. Lett.* **15** 226
[4] Lin X, Yang W, Wang K L and Zhao W 2019 Two-dimensional spintronics for low-power electronics *Nat.Electron.* **2** 274–83
[5] Streubel R, Fischer P, Kronast F, Kravchuk V P, Sheka D D, Gaididei Y, Schmidt O G and Makarov D 2016 Magnetism in curved geometries *J. Phys. D: Appl. Phys.* **49** 363001
[6] Vedmedenko E Y *et al* 2020 The 2020 magnetism roadmap *J. Phys. D: Appl. Phys.* **53** 453001
[7] Sheka D D 2021 A perspective on curvilinear magnetism *Appl. Phys. Lett.* **118** 230502
[8] Sheka D D, Pylypovskyi O V, Landeros P, Gaididei Y, Kákay A and Makarov D 2020 Nonlocal chiral symmetry breaking in curvilinear magnetic shells *Commun. Phys.* **3** 128
[9] Sanchez-Valencia J R, Longtin R, Rossell M D and Gröning P 2016 Growth assisted by glancing angle deposition: a new technique to fabricate highly porous anisotropic thin films *ACS Appl. Mater. Interfaces* **8** 8686–93
[10] Fernández-Pacheco A, Skoric L, María De Teresa J, Pablo-Navarro J, Huth M and Dobrovolskiy O V 2020 Writing 3D nanomagnets using focused electron beams *Materials* **13** 3774
[11] Fomin V M, Smith E J, Makarov D, Sanchez S and Schmidt O G 2011 Dynamics of radial-magnetized microhelix coils *Phys. Rev. B* **84** 174303
[12] Wang Y, Ma Z, Chen Y, Zou M, Yousaf M, Yang Y, Yang L, Cao A and Han R P S 2016 Controlled synthesis of core-shell carbon@MoS_2 nanotube sponges as high-performance battery electrodes *Adv. Mater.* **28** 10175–81

[13] Tiwari A P, Yoon Y, Novak T G, Azam A, Lee M, Lee S S, Lee G-hyoung, Srolovitz D J, An K-S and Jeon S 2019 Lattice strain formation through spin-coupled shells of MoS_2 on Mo_2C for bifunctional oxygen reduction and oxygen evolution reaction electrocatalysts *Adv. Mater. Interfaces* **6** 1900948
[14] Caha I *et al* 2025 One-dimensional CrI_3 encapsulated within multi-walled carbon nanotubes *Commun. Chem.* **8** 155
[15] Kaneda M *et al* 2025 Tunable-diameter nanoscrolls from Janus $WSSe/WSe_2$ heterostructures *ACS Nano* **19** 34918–27
[16] Li J-W, Su G and Gu B 2025 Ferromagnetic semiconductor nanotubes with room Curie temperatures *npj Comput. Mater.* **11** 292
[17] He W, Yin Y, Gong Q, Evans R F L, Gutfleisch O, Xu B X, Yi M and Guo W 2023 Giant magnetocaloric effect in magnets down to the monolayer limit *Small* **19** e2300333
[18] Yue Y, Wang B, Miao N, Jiang C, Lu H, Zhang B, Wu Y, Ren J and Wang M 2021 Tuning the magnetic properties of Zr_2N mxene by biaxial strain *Ceram. Int.* **47** 2367–73
[19] Perfetti M *et al* 2018 Magnetic anisotropy switch: easy axis to easy plane conversion and vice versa *Adv. Funct. Mater.* **28** 1801846
[20] Raza A and Perfetti M 2023 Electronic structure and magnetic anisotropy design of functional metal complexes *Coord. Chem. Rev.* **490** 215213
[21] Moaied M and Hong J 2019 Size-dependent critical temperature and anomalous optical dispersion in ferromagnetic CrI_3 nanotubes *Nano (Basel)* **9** 153
[22] Edstrom A, Amoroso D, Picozzi S, Barone P and Stengel M 2022 Curved magnetism in CrI_3 *Phys. Rev. Lett.* **128** 177202
[23] Safi A L, Chakraborty S, Ahmed Md A and Chattopadhyay B 2022 Strain tunable electronic band structure and magnetic anisotropy of CrI_3 bilayer *ECS J. Solid State Sci. Technol.* **11** 063008
[24] Kuklin A V, Visotin M A, Baek W and Avramov P V 2020 CrI_3 magnetic nanotubes: a comparative DFT and DFT + U study and strain effect *Physica E* **123** 114205
[25] McGuire M A, Dixit H, Cooper V R and Sales B C 2015 Coupling of crystal structure and magnetism in the layered, ferromagnetic insulator CrI_3 *Chem. Mater.* **27** 612–20
[26] Chakraborty S and Ravikumar A 2021 Substrate induced electronic phase transitions of CrI_3 based van der waals heterostructures *Sci. Rep.* **11** 198
[27] Ren J T, Feng Y, Ke S S and Lü H F 2023 Tunable quantum anomalous Hall gap in compressed graphene/CrI_3 van der Waals heterostructures *Adv. Phys. Res.* **4** 2300026
[28] Yang S *et al* 2023 Controlling the 2D magnetism of $CrBr_3$ by van der Waals stacking engineering *J. Am. Chem. Soc.* **145** 28184–90
[29] Persson K 2014 Materials data on $CrBr_3$ (sg:148) by materials project, An optional note.
[30] Ma P, Shu J, Zhao X, Cao Y, Wang L, Chen G, Wu J and Mi. Y 2023 The $CrBr_3$ monolayer: two dimension sodium ion battery anode material to characterize state-of-charge by magnetism *Appl. Surf. Sci.* **623** 157074
[31] Lu S *et al* 2023 Controllable dimensionality conversion between 1D and 2D $CrCl_3$ magnetic nanostructures *Nat. Commun.* **14** 2465
[32] Wang J, Ahmadi Z, Lujan D, Choe J, Taniguchi T, Watanabe K, Li X, Shield J E and Hong X 2023 Physical vapor transport growth of antiferromagnetic $CrCl_3$ flakes down to monolayer thickness *Adv. Sci.* **10** 2203548
[33] Persson K 2016 Materials data on $CrCl_3$ (sg:148) by materials project, An optional note.
[34] Webster L and Yan J-A 2018 Strain-tunable magnetic anisotropy in monolayer $CrCl_3$, $CrBr_3$ and CrI_3 *Phys. Rev. B* **98** 144411
[35] Kohn W and Sham L J 1965 Self-consistent equations including exchange and correlation effects *Phys. Rev.* **140** A1133–8
[36] Hohenberg P and Kohn W 1964 Inhomogeneous electron gas *Phys. Rev.* **136** B864–71
[37] Kresse G and Hafner J 1993 Ab initio molecular dynamics for liquid metals *Phys. Rev. B* **47** 558–61
[38] Kresse G and Hafner J 1994 Ab initio molecular-dynamics simulation of the liquid-metal-amorphous-semiconductor transition in germanium *Phys. Rev. B* **49** 14251–69
[39] Kresse G and Furthmüller J 1996 Efficiency of ab-initio total energy calculations for metals and semiconductors using a plane-wave basis set *Comput. Mater. Sci.* **6** 15–50
[40] Kresse G and Furthmüller J 1996 Efficient iterative schemes for ab initio total-energy calculations using a plane-wave basis set *Phys. Rev. B* **54** 11169–86
[41] Perdew J P, Chevary J A, Vosko S H, Jackson K A, Pederson M R, Singh D J and Fiolhais C 1993 Erratum: atoms, molecules, solids and surfaces: applications of the generalized gradient approximation for exchange and correlation *Phys. Rev. B.* **48** 4978
[42] Perdew J P, Burke K and Ernzerhof M 1996 Generalized gradient approximation made simple *Phys. Rev. Lett.* **77** 3865–8
[43] Blöchl P E 1994 Projector augmented-wave method *Phys. Rev. B* **50** 17953–79
[44] Kresse G and Joubert D 1999 From ultrasoft pseudopotentials to the projector augmented-wave method *Phys. Rev. B* **59** 1758–75